PAPER • OPEN ACCESS

Experimental investigation of unsteady convective heat transfer under airflow velocity and temperature variations

View the article online for updates and enhancements.

Experimental investigation of unsteady convective heat transfer under airflow velocity and temperature variations

Stefan Brack* , Rico Poser and Jens von Wolfersdorf

Institute of Aerospace Thermodynamics (ITLR), University of Stuttgart, Pfaffenwaldring 31, D-70569 Stuttgart, Germany

E-mail: itlr@itlr.uni-stuttgart.de

CrossMark

Abstract
An experimental approach to study unsteady local heat transfer characteristics due to airflow velocity and/or airflow temperature variations is presented. It uses controlled electrical heaters and rotating vanes to independently vary the flow and thermal boundary conditions. Time-resolved surface temperatures are measured using an *in situ* calibrated infrared thermography camera. Those surface temperatures are analyzed by modeling the transient conjugate heat transfer process in the wall to obtain locally resolved surface heat flux distributions. The applicability is illustrated for a flow and heat transfer behind a tetrahedral vortex generator on a flat plate.

Keywords: conjugate, convective, transient heat transfer, 3D heat conduction, vortex generator, infrared

(Some figures may appear in colour only in the online journal)

1. Introduction

Unsteady heat transfer processes are an intrinsic part of gas turbines. They occur due to the operating principle itself, changing heat loads, varying cooling air mass flows and unsteady flow phenomena. In addition, for stationary gas turbines the increasing amount of renewable energy leads to a higher proportion of unsteady operating conditions with frequent start-up and shut-down processes as well as operation in different partial load conditions (Magni *et al* 2016, Kuželka *et al* 2019, Abudu *et al* 2021). Hence, unsteady heat transfer processes are an area of great interest and will gain further importance in the future. To ensure even safer and more efficient operation under transient conditions, it is of particular interest to numerically and experimentally generate, capture and evaluate the effects of these operating conditions on gas turbine cooling.

To experimentally study unsteady heat transfer, an experimental setup is required that allows a controlled and repeatable variation of the boundary conditions. In case of airflows, many researches applied a mesh heater to change the airflow temperature (Ireland *et al* 1999, Newton *et al* 2003, Poser *et al* 2005, Liu *et al* 2014). This type of heater is characterized by a homogeneous temperature field over the entire cross-section and responds quickly to changes due to their low thermal mass.

To vary the airflow velocity, a wide variety of designs exist and were applied in experimental studies already. All designs use either a volume change or a cross section change to vary the flow velocity. Volume change designs use adjustable reservoirs which are connected to the main flow path. The volume change is achieved by, for example, a piston (Fallen 1982, Park *et al* 1982), a membrane pump (Persoons *et al* 2012) or a sub-woofer membrane (Moon *et al* 2005, Ji *et al* 2008, Lalizel *et al* 2012, Li *et al* 2013). The cross-section change can be realized with a rotating valve (Sheriff and Zumbrunnen 1994, Habib *et al* 2002, Zohir *et al* 2005, Elshafei *et al* 2008), a sliding gate

---

* Author to whom any correspondence should be addressed.

valve (Galoul *et al* 2010), a critical flow cross-section (Durst *et al* 2003, Ünsal and Durst 2006) or vanes arranged above each other (Gompertz *et al* 2011, Jensen *et al* 2011, Liu *et al* 2015).

The choice of the applied temperature measurement equipment determines the applicable evaluation methods for the heat transfer. Often thermocouples are used in the fluid as well as on the surface. In the few works that spatially resolve the heat transfer, an infrared (IR) camera provides surface temperature data (Coulthard *et al* 2007, Bons 2009, Bons *et al* 2009). In addition to the spatial resolution, the IR camera also offers a temporal resolution of the surface temperature, which significantly expands the range of evaluation methods that can be used. These methods use numerical or analytical models of the three-dimensional heat conduction equation within the solid.

The present work presents an approach to experimentally perform, measure and evaluate time-resolved convective heat transfer using a transient conjugate analysis. A developed airflow control system allows an independent adjustment and change of the airflow temperature and the airflow velocity. High-accuracy surface temperature measurements with spatial and temporal resolution are achieved by an *in situ* calibration of the IR camera. The applied evaluation method provides a temporally and spatially resolved surface heat flux and considers 3D heat conduction effects in the solid. Two different experimental results verify the performance of the experimental approach.

2. Experimental approaches

2.1. Experimental setup

Figure 1 shows a sketch of the experimental setup. Air from the ambient is sucked through the experimental setup with the aids of a roots vacuum pump operating at a constant rotational speed. First, the air flows through a dust filter (A). Then it gets through a mesh heater (B) and enters the Perspex test section (C) ($\rho_s = 1190 \, \mathrm{kg \, m^{-3}}$, $c_s = 1470 \, \mathrm{J \, (kg \, K)^{-1}}$, $k_s = 0.19 \, \mathrm{W \, (m \, K)^{-1}}$). Directly downstream the test section follow adjustable vanes (I), arranged above each other, and the piping system (J) connecting the experimental setup to the roots vacuum pump.

The test section with its 0.03 m thick Perspex walls has a total length of 1.02 m and a rectangular, inner cross section area of $0.12 \times 0.15 \, \mathrm{m^2}$. Inside the test section a 0.03 m thick and 0.12 m wide flat plate (G) is mounted in its symmetry plane and splits up the single channel into two sub-channels. This design ensures an adiabatic boundary condition inside the symmetry plane of the flat plate.

The flat plate is made out of Perspex too. On its top surface the unsteady heat transfer in the wake region of a full body tetrahedral vortex generator (VG) is investigated. Figure 2 shows the position, the geometrical dimensions as well as the induced vortex systems of the VG. It has a height H_{vg} of 26 mm. The length and the width W_{vg} are identical with 65 mm. To get a symmetrical flow field above and below the plate, on each side a single VG has been mounted.

The complex flow field with up- and downwash regions of the longitudinal vortices leads to a complex heat transfer pattern. Starting at the tip, the two main vortices lead to two streaks of high heat transfer in their downwash regions. The corner vortices arise at the two sharp ends of the VG. In between a main vortex and its corresponding corner vortex a so-called upwash region leads to a particular streak of low heat transfer. In addition, around the VG a horseshoe vortex is induced. A typical heat transfer pattern in the wake of the VG is visualized in figure 2 (top view). Blue areas represent regions with low heat transfer and yellow areas represent regions with high heat transfer.

The top wall of the test section includes three openings for IR radiation transmitting windows (F) which enables flexible access for the IR camera (H) to capture the surface wall temperature at different locations of the flat plate. As IR transmitting window material serves calcium fluoride (CaF_2). It reaches with its thickness of 0.005 m a transmittance of 95% in the sensitive wavelength range from 1.5 to 5.1 μm of the applied IR camera[1].

Additionally, the test section top wall includes 0.205 m upstream the leading edge of the flat plate a port for hot-wire anemometry and thermometry[2] (D). The hot-wire system measures locally the temporally varying inlet conditions (inlet velocity u_{in}, inlet temperature $T_{f,in}$). Due to the installation situation, the orientation of the two single-sensor probes with a wire diameter of 10 μm is $90°$. One probe operates in constant temperature mode (CTA) and measures the airflow velocity. The other probe operates in constant current mode (CCT) and measures the local airflow temperature.

Further downstream above the flat plate, fine wire thermocouples (E) with a wire diameter of 80 μm measure the local airflow temperature at mid channel height.

### 2.2. Airflow control system

The mesh heater together with its two DC power supply units and the adjustable vanes are the two components of the airflow control system and enclose the test section. If one of the two control variables heater voltage U_H or angle of attack of the vanes Ω is changed, the pressure drop on the flow path to the vacuum pump changes and thus also the airflow velocity u and airflow temperature T_f within the test section. In conclusion, a controlled variation of the airflow velocity or airflow temperature requires a necessary controlled change of U_H as well as Ω.

The mesh heater itself is built up with six steel meshes, arranged one after the other downstream and with a square cross-sectional area of $0.19 \times 0.19 \, \mathrm{m^2}$, a mesh width of 40 μm and a wire diameter of 25 μm.

Downstream the test section three adjustable vanes are placed above each other. By varying the angle of attack Ω at the same time, the gap between the vanes and to the lower and upper wall varies and so does the pressure drop. Each 0.01 m

---

[1] FLIR SC7600.

[2] SVMtec hot-wire system eCTA and eCCA with probe type HWP10/90.
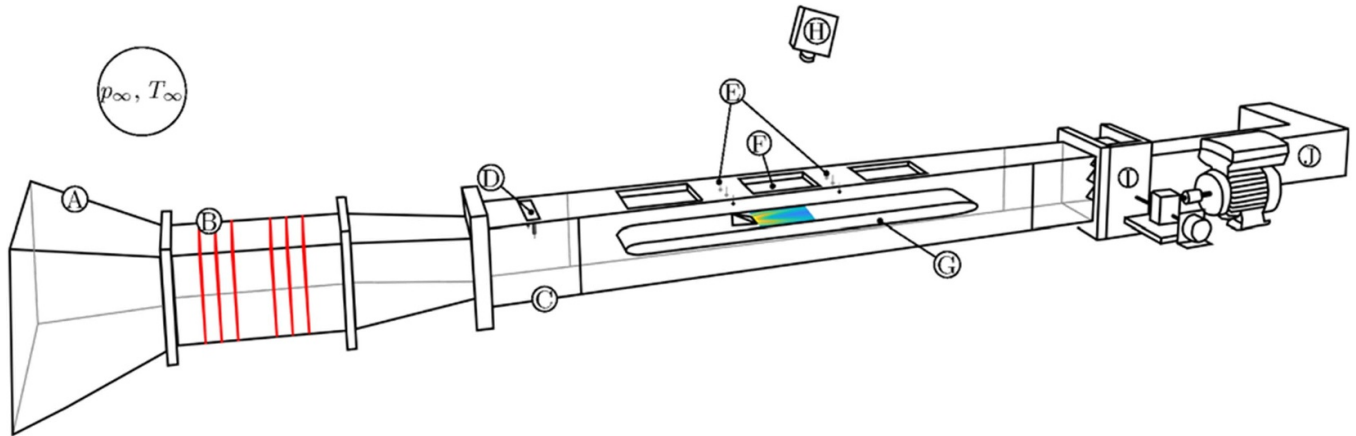
Figure 1. Test facility (legend: (A) dust filter, (B) mesh heater, (C) test section, (D) hot-wire probes, (E) fine-wire thermocouples, (F) IR transmitting window, (G) flat plate, (H) IR camera, (I) adjustable vanes, (J) piping system).
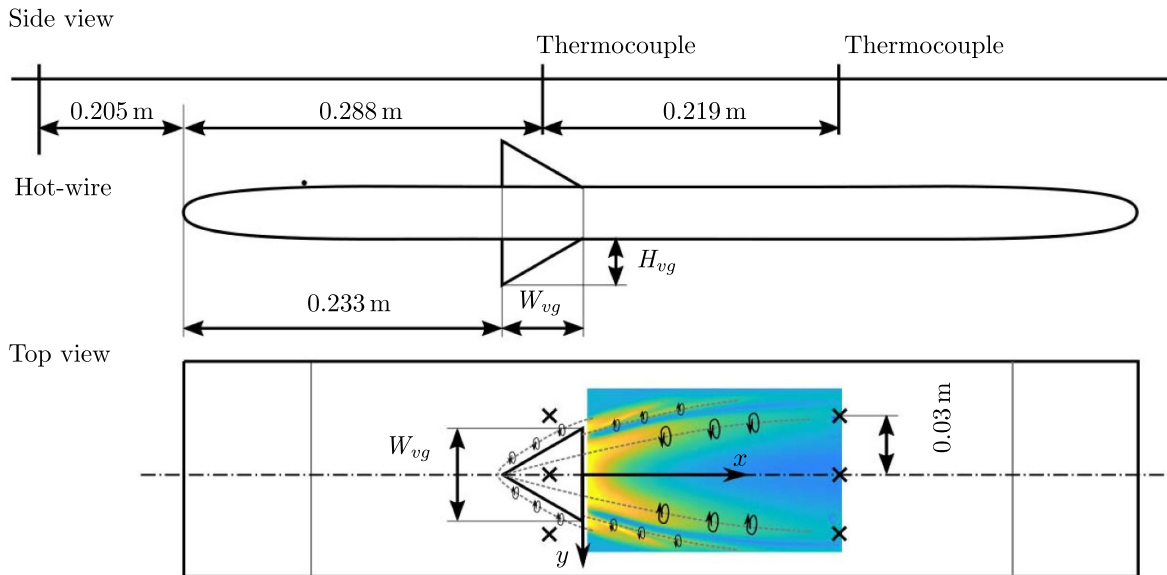
Figure 2. Sketch of vortex generator arrangement with typical local heat transfer distribution in the wake of the vortex generator.

thick vane has a wingspan of 0.12 m and a chord length of 0.049 m. All blades are connected by gears to the same shaft, which is driven by an electric motor via a reduction gearbox. A picture of the complete assembly is shown in figure 3.

With the aid of a PI controller the measured Ω is used to vary the rotational speed of the electric motor and therefore to control Ω. An automatic calibration in three steps, shown in figure 4, assigns the measured Ω^* to the actual Ω. In the first step, the measured Ω_1^* is set to zero in an arbitrary fixed position. Then the vanes are rotated by $200°$ at constant speed. At the same time, the hot-wire probe records u_{in} as a function of Ω_1^*. When Ω_1^* reaches the position of the minimum gap between the vanes, a sharp minimum of u_{in} is obtained, which can be determined exactly. The vane angle Ω to this minimum is defined as $90°$ and provides the assignment of Ω_2^* to Ω.

The second step of calibration optimizes the obtained assignment of Ω_2^* to Ω with additional measurements of u_{in} at different angles and non rotating vanes. Between $80°$ and

$100°$, u_{in} is measured with a resolution of $1.25°$. The minimum obtained in this step is considered as exact for the assignment of Ω^* to Ω.

While the first two steps provide the exact assignment of Ω^* and Ω, the third step of calibration determines the characteristics of u_{in} versus Ω. For Ω greater than $140°$, u_{in} hardly changes at all. So only the range between $90°$ and $140°$ is used for experiments.

The airflow control system aims to reproducibly control the individual histories of u_{in} and $T_{f,in}$ for each experiment by continuously changing U_H and Ω. However, since the physical relationship

$$(u_{in}, T_{f,in}) = (U_H, \Omega) \tag{1}$$

is not linear and the response time of the airflow control system devices is hardly faster than the desired changes, a PID controller cannot be used to control the process variables u_{in}
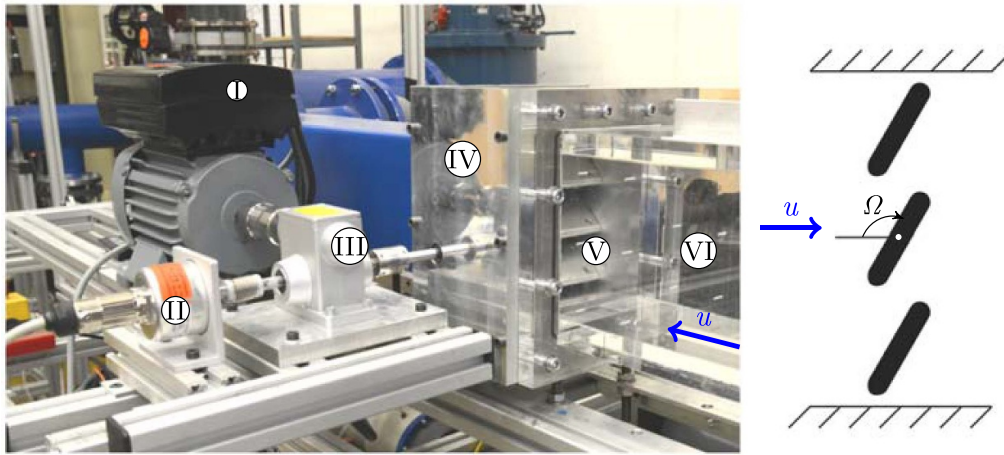
Figure 3. Adjustable vanes mechanism (legend: (I) asynchronous electric motor, (II) optical singleturn shaft encoder, (III) worm gearbox, (IV) gearbox, (V) vanes, (VI) test section).

(a) Step 1   (b) Step 2   (c) Step 3
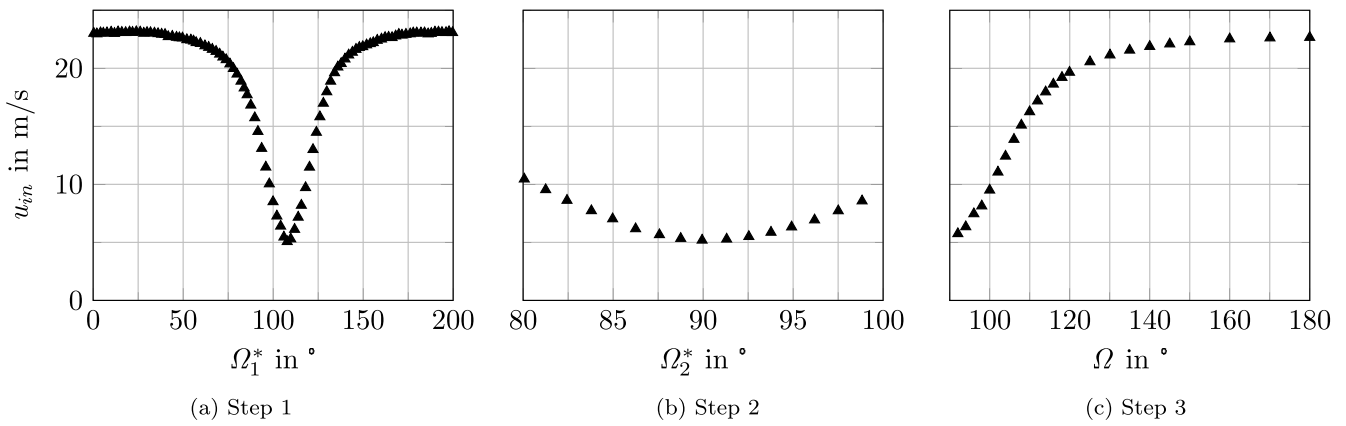
Figure 4. Initial calibration of the adjustable vanes.

and $T_{f,in}$. For this reason, a steady-state operating range is experimentally determined and serves as the basis to calculate U_H and Ω from the required course of u_{in} and $T_{f,in}$. In the steady-state case, two equations describe the physical relationship between the control variables and the process variables. On the one hand the steady and incompressible Bernoulli equation

$$p_\infty = p_{in} + \frac{1}{2}\rho_{f,in}\left(1 + \zeta_H\right)u_{in}^2 \tag{2}$$

with a Reynolds number dependent loss coefficient ζ_H for the mesh heater from the ambient (p_∞, T_∞) to the inlet section provides a connection. On the other hand, the energy equation

$$\dot{m}_f c_{p,f}\left(T_{f,in} - T_{f,\infty}\right) = P_H \tag{3}$$

defines the influence of the heater power on the flow variables at the inlet. If these equations are further transformed using Ohm's law

$$P_H = \frac{U_H^2}{R_H} \tag{4}$$

and the ideal gas equation

$$p = \rho_f R_{s,f} T_f, \tag{5}$$

the following approximate relationships are obtained:

$$\frac{1}{u_{in}^2} \propto f\left(\frac{1}{T_{f,in}}\right), \quad \Omega = \text{const.} \tag{6}$$

$$\frac{T_{f,in} - T_\infty}{u_{in}} \propto f\left(U_H^2\right), \quad \Omega = \text{const.} \tag{7}$$

While R_H represents the constant heater mesh resistance, $R_{s,f}$ is the specific gas constant for dry air.

By determining the required U_H to reach different temperature levels for different Ω and then plotting the measured data against each other as in the two equations (6) and (7), one obtains the figures 5 and 6. Both figures visualize the functional relationship which is linearly approximated. In conclusion, the operating range is mathematically described and can be used to calculate U_H and Ω for predefined histories of u_{in} and $T_{f,in}$ in advance. The procedure to calculate the histories of Ω and U_H was implemented in LabVIEW™ with a stochastic solver for systems of non-linear equations. The coefficients for
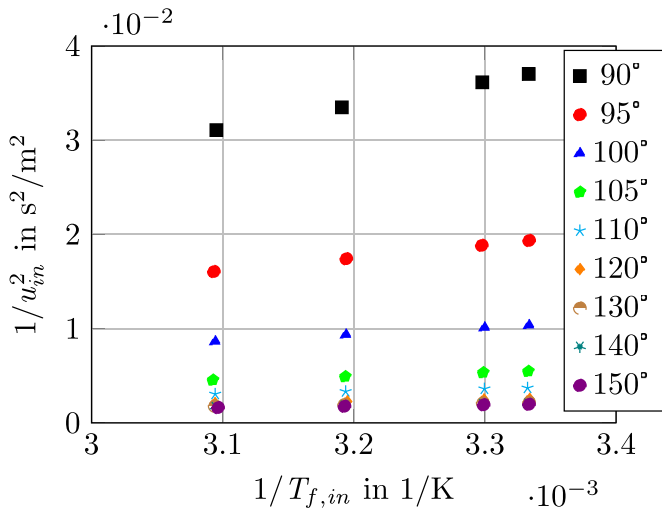
Figure 5. Measured physical relationship according to equation (6) using Bernoulli equation.
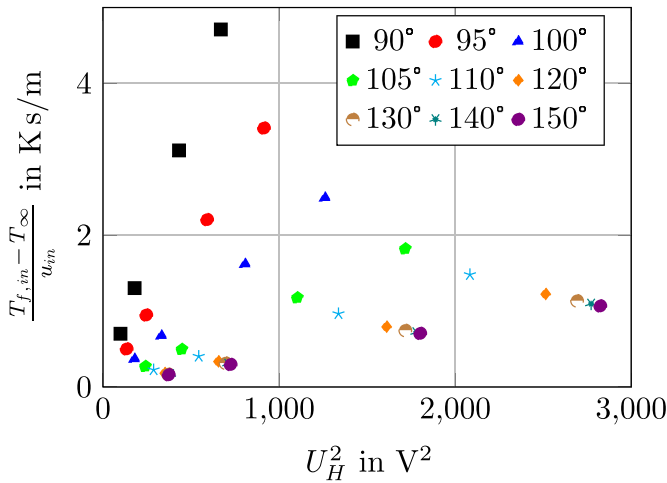

Figure 6. Measured physical relationship according to equation (7) using Energy balance.

the linear approximations are interpolated with a spline interpolation.

2.3. Inlet velocity profiles

During each experiment Ω varies according to the required histories of u_{in} and $T_{f,in}$. As the flow velocities in the channel are in areas significantly below the speed of sound, these geometric changes at the outlet might also change the velocity profile in front of the flat plate and above the flat plate. To exclude such an influence, the velocity profile at the inlet was traversed for different vane angles. Figure 7 shows the profiles normalized with the mean velocity $\bar{u}$ over the channel height for different Ω. The inlet profile is independent of Ω.

Two aspects cause a non-symmetrical velocity profile. First, the reduction of the cross-section between the mesh heater and the test section (see figure 1). Second, the traversing procedure has an influence. During the acquisition of the
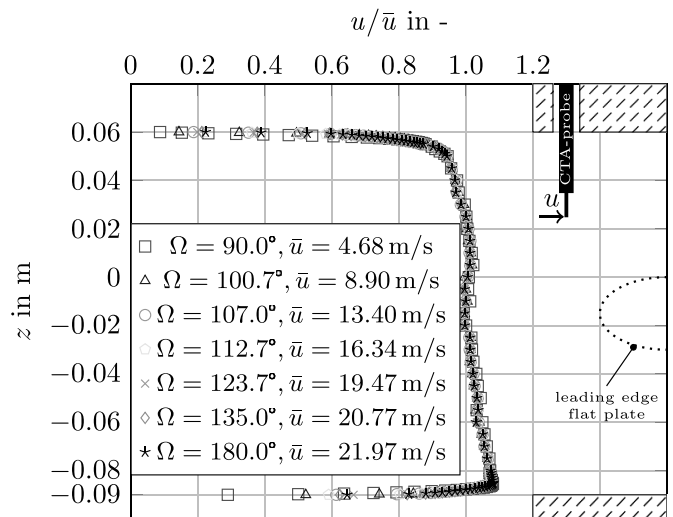

Figure 7. Normalized vertical velocity profiles at channel inlet.

velocity profiles, the probe was pulled back stepwise to the probe ports.

The measurement of the velocity profile at two further positions perpendicular to the main airflow direction (0.03 and -0.03 m) yielded the same result as the profiles shown in figure 7 for the center of the channel.

Independent of Ω, the local velocity measured at $z = 0.02$ m always corresponds to $\bar{u}$. This fixed position was selected for the experiments and the measured local velocity has been defined as u_{in}.
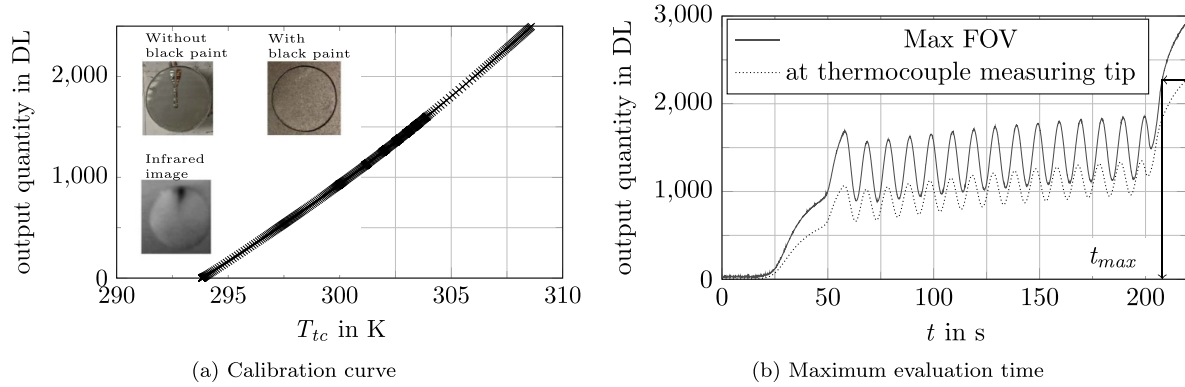
2.4. In situ *calibration of IR camera*

As shown in figure 1, an IR camera captures the surface temperature of the evaluation area with temporal and spatial resolution. Many influencing factors, such as ambient radiation, transmittance of the window and emittance of the observed surface influence the measurement result. Therefore, each of these quantities would have to be known exactly in order to get accurate surface temperature measurements with the IR camera. In order to take all these factors into account and to obtain quantitative measurement results, the IR camera was calibrated *in situ* with the aid of one type T surface thermocouple[3] in the field of view (FOV). The graph of figure 8(a) includes three pictures in top view of the surface thermocouple glued[4] on a perspex cylinder and mounted into the flat plate. The top left picture shows the cylinder with surface thermocouple without black paint coating[5]. The top right picture shows again the same cylinder with black paint coating. The complete flat plate as well as the cylinder and the surface thermocouple are coated with black paint in order to get a homogeneous emittance of the surface. The bottom left picture represents a detail of one IR image during an experiment. One can distinguish

---

[3] Omega™ CO2-T.

[4] Omegabond OB101-2.

[5] Hallcrest type SPB100.

(a) Calibration curve

(b) Maximum evaluation time

Figure 8. Exemplary *in situ* calibration data of the IR camera.

the copper leg of the thermocouple from the surrounding. Due to different material properties of copper ($\rho = 8920$ kg m^{-3}, $c = 385.1$ J (kg K)$^{-1}$, $k = 377.05$ W (m K)$^{-1}$) compared to constantan ($\rho = 8920$ kg m^{-3}, $c = 393.5$ J (kg K)$^{-1}$, $k = 21.1$ W (m K)$^{-1}$) and Perspex, the local temperature of the copper leg rises more slowly.

For the evaluation area the experimentally determined heat transfer coefficient is always lower than 200 W (m^2 K)$^{-1}$. Together with the average thermal conductivity k_{tc} of 199.08 W (m K)$^{-1}$ and the thickness L_{tc} of 10 μm, this leads to a Biot number ($Bi = hL_{tc}/k_{tc}$) smaller than 2.5×10^{-6}. Hence, the assumption of a homogeneous measuring tip temperature of the thermocouple is justified (lumped body assumption).

The graph of figure 8(a) shows an exemplary calibration curve received from a single experiment. The experiment started with an airflow temperature increase from ambient conditions to a higher temperature level. Then an airflow temperature pulsation with a frequency of 0.1 Hz is superimposed. At the end the airflow temperature as well as the airflow velocity have been increased to their maximum values.

To obtain the calibration curve, the radiation measured locally above the measuring tip of the surface thermocouple is plotted against the measured temperature of the surface thermocouple T_{tc}. The output quantity of the IR camera is given in Digital Level DL. The maximum detected radiation of a pixel in the FOV of the IR camera as well as the measured radiation at the measuring tip of the thermocouple are plotted against t in the graph of figure 8(b). Due to the varying heat transfer distribution over the surface, both histories differ from each other.

The airflow temperature and airflow velocity increase at the end of the experiments leads to a strong temperature and radiation increase at the measuring tip. Thus, this final sequence of the experiment enables a wide span of measured radiation at the measuring tip of the surface thermocouple and the longest possible evaluation time t_{max}.

3. Evaluation method

The previous sections focused on the generation and acquisition of the unsteady convective heat transfer situation. Another main object is the temporally and spatially resolved evaluation of the heat transfer situation schematically visualized in figure 9. For the evaluation the method according to Estorf (2006) was applied. This method is based on the analytical evaluation of the transient three-dimensional heat transfer equation within the wall

$$\frac{\partial T_s}{\partial t} = \underbrace{\frac{k_s}{\rho_s c_s}}_{\alpha_s} \left[\frac{\partial^2 T_s}{\partial x^2} + \frac{\partial^2 T_s}{\partial y^2} + \frac{\partial^2 T_s}{\partial z^2} \right] \tag{8}$$

for constant material properties. Estorf (2006) also shows that linear temperature dependent material properties of the wall, resulting in a temperature dependent thermal diffusivity α_s, can be taken into account with a Kirchhoff transformation. A transient surface heat flux

$$z = 0: \quad -k_s \left. \frac{\partial T}{\partial z} \right|_{z=0} = \dot{q}_w(t) \tag{9}$$

captures the heat transfer at the interface between fluid and solid.

As special requirements for the experimental setup and the experimental procedure, on the one hand the entire setup has to be in thermal equilibrium

$$t = 0: \quad T = T_0 \tag{10}$$

at the beginning of the experiment. On the other hand, the wall in z-direction is considered to be semi-infinite

$$z \to +\infty: \quad T = T_0. \tag{11}$$

This condition can be sufficiently realized by limiting the experiment duration t_d

$$t_d < \frac{L^2}{16} \frac{\rho_s c_s}{k_s} \tag{12}$$

according to Schultz and Jones (1973). It ensures for a one dimensional heat conduction situation with an initial step change of $\dot{q}_w$, a temperature change at the penetration depth $z = L$ of less than 1% compared to the surface temperature change.
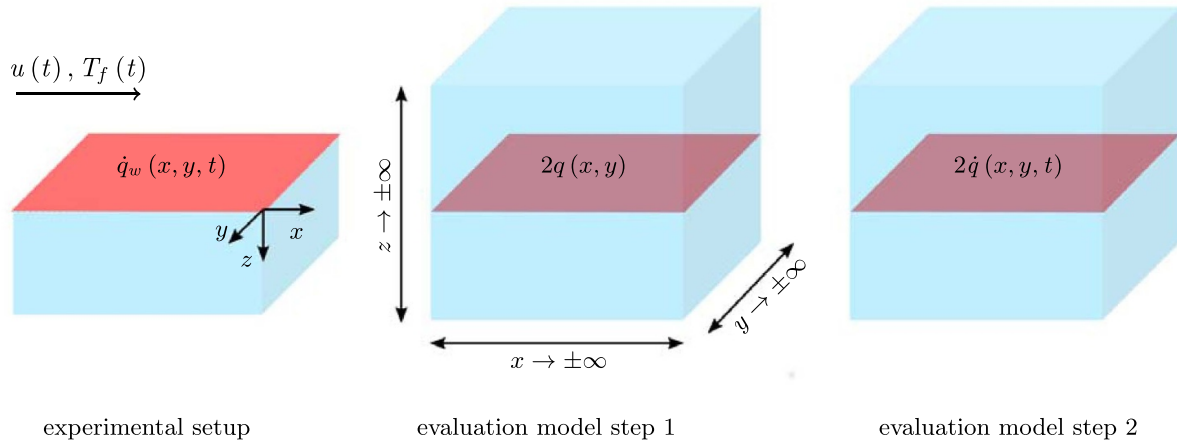
Figure 9. Evaluation model according to Estorf (2006).

To find an analytical solution for the heat transfer situation of the experimental setup, Estorf (2006) considered a similar situation in the first step (figure 9, evaluation model step 1). However, this similar situation only contains heat conduction processes. For this heat conduction problem within an infinite cube with an initial heat release $2q(x,y,z=0)$ in the xy-plane, an analytical solution exists in the Fourier space

$$\tilde{\theta}(u,v,z,t) = \frac{1}{\rho_s c_s \sqrt{\pi \alpha_s t}} q(u,v)$$
$$\times \exp\left[-\alpha_s\left(u^2 + v^2\right)t - \frac{z^2}{4\alpha_s t}\right]. \qquad (13)$$

The frequencies u and v belong to the respective spatial directions x and y and $\tilde{\theta}$ represents the normalized temperature $\theta = T_s - T_0$ in Fourier space. In order to consider the symmetry to the xy-plane and to apply the obtained results to the experimental setup, the initial heat release contains the factor two.

Using the Duhamel principle (figure 9, evaluation model step 2), Estorf (2006) transformed the solution obtained for the initial condition of an initial heat release into a wall temperature field

$$\tilde{\theta}(u,v,z,t) = \frac{1}{\rho_s c_s \sqrt{\pi \alpha_s}} \int_0^t \dot{q}(u,v,\tau)$$
$$\times \frac{\exp\left[-\alpha_s\left(u^2 + v^2\right)(t-\tau) - \frac{z^2}{4\alpha_s(t-\tau)}\right]}{\sqrt{t-\tau}} d\tau \qquad (14)$$

for a time-dependent heat flux $2\dot{q}(x,y,z=0)$ in the xy-plane. For example, Özisik (1985) explains the Duhamel principle in detail. The inverse of the temperature is

$$\dot{q}(u,v,t) = \frac{k_s}{\sqrt{\pi \alpha_s}}$$
$$\times \int_0^t \frac{\partial\left[\tilde{\theta}(u,v,z=0,\tau)\,\mathrm{e}^{\left[-\alpha_s\left(u^2+v^2\right)(t-\tau)\right]}\right]}{\partial \tau}$$
$$\times \frac{1}{\sqrt{t-\tau}} d\tau \qquad (15)$$

and corresponds to the surface heat flux $\dot{q}_w$ of the experimental setup in the Fourier space.

A numerical approximation of the surface temperature T_w is necessary to solve the integral of equation (15). Applying the piecewise linear approximation of T_w

$$t_i < \tau < t_{i+1}:$$
$$T_w(\tau) = \frac{T_w(t_{i+1}) - T_w(t_i)}{t_{i+1} - t_i}(\tau - t_i) + T_w(t_i) \qquad (16)$$

with a constant time step Δt leads to the finite sum of the surface heat flux in Fourier space

$$\dot{q}_{w,lm}^n = k_s \sum_{k=0}^{n-1}\left\{\left[\left(\frac{1}{2\,\omega_{lm}\alpha_s} + \omega_{lm}(t_n - t_k)\right)\right.\right.$$
$$\times \frac{\tilde{\theta}_{w,lm,k+1} - \tilde{\theta}_{w,lm,k}}{\Delta t} + \omega_{lm}\tilde{\theta}_{w,lm,k}\right]$$
$$\times \left(\mathrm{erf}[f_{lm}(t_k)] - \mathrm{erf}[f_{lm}(t_{k+1})]\right)$$
$$+ \frac{\tilde{\theta}_{w,lm,k+1} - \tilde{\theta}_{w,lm,k}}{\sqrt{\pi \alpha_s}\Delta t}\left(\sqrt{t_n - t_k}\,\mathrm{e}^{-\alpha_s\omega_{lm}^2(t_n - t_k)}\right.$$
$$\left.\left. - \sqrt{t_n - t_{k+1}}\,\mathrm{e}^{-\alpha_s\omega_{lm}^2(t_n - t_{k+1})}\right)\right\}. \qquad (17)$$

The discrete frequencies u_l and v_m result from the uniform discretization (L pixel $\times$ M pixel) of the evaluated surface and appear in equation (17) with the terms $\omega_{lm} = \sqrt{u_l^2 + v_m^2}$ and $f_{lm}(\tau) = \omega_{lm}\sqrt{\alpha_s(t_n - \tau)}$. The indices l and m relate to the

discretization (pixel-wise) in x- and y-direction. The superscript n is the discrete time point of the evaluation of $\dot{q}_{w,lm}^n$. Using a cosine transformation to calculate the normalized surface temperature $\tilde{\theta}_w$ instead of a Fourier transformation leads to adiabatic sidewalls at the borders of the evaluated area. An inverse Fourier transformation or cosine transformation respectively delivers the spatially and temporally resolved surface heat flux $\dot{q}_w(x,y,t)$.

The spatially and temporally resolved heat transfer coefficient results from the application of the Newton's law of cooling

$$h(x,y,t) = \frac{\dot{q}_w(x,y,t)}{T_w(x,y,t) - T_{ref}(x,y,t)} \qquad (18)$$

in a post processing step.

The reference temperature T_{ref} within this study is the free stream temperature resolved in time and space. To get the complete T_{ref}-field, the interpolation method according to Poser and von Wolfersdorf (2011) has been applied.

The influence of spatial and temporal discretization has been discussed by Estorf (2006). A comparison to heat transfer measurements using narrowband thermochromic liquid crystals is given in Brack *et al* (2017).

4. Uncertainty analysis

The evaluation quantities $\dot{q}_w$ and h are affected by the uncertainty of the measurement quantities. Calibration procedures enable to determine the uncertainty of the measurement quantities which are given in table 1. For the applied thermocouples a stationary calibration was carried in a calibrated dry block calibrator[6]. The CTA hot-wire probe is calibrated by the manufacturer, the CCT probe is calibrated *in situ*. A calibrated fine wire thermocouple, placed next to the CCT probe, provides the measurement values for the *in situ* calibration during the determination of the operating range of the experimental setup.

The method according to Moffat (1982) has been used to calculate the uncertainties of the evaluation quantities. Applying this method to $\dot{q}_w$ in Fourier space leads to the following equation for the uncertainty of the surface heat flux amplitudes

$$\begin{aligned} \delta\dot{q}_{w,lm}^n = \Bigg(&\sum_{k=0}^{n-1} \left(\frac{\partial \dot{q}_{w,lm}^n}{\partial \tilde{\theta}_{lm}^k}\right)^2 \left[\delta\tilde{\theta}_{lm}^k\right]^2 \\ &+ \left(\frac{\partial \dot{q}_{w,lm}^n}{\partial \omega_{lm}}\right)^2 [\delta\omega_{lm}]^2 + \left(\frac{\partial \dot{q}_{w,lm}^n}{\partial \rho_s}\right)^2 [\delta\rho_s]^2 \\ &+ \left(\frac{\partial \dot{q}_{w,lm}^n}{\partial c_s}\right)^2 [\delta c_s]^2 + \left(\frac{\partial \dot{q}_{w,lm}^n}{\partial k_s}\right)^2 [\delta k_s]^2 \Bigg)^{1/2}. \end{aligned} \qquad (19)$$

An inverse Fourier transform yields then $\delta\dot{q}_w$.

To obtain the uncertainty of the heat transfer coefficient δh, Moffat's method was applied too and results in

[6] AMETEK RTC-159B.

Table 1. Independent input quantities with their typical measured values and standard deviation.

Qty	Meas. range	Std. dev. δx_i
u_0	5–25 m s^{-1}	0.1 m s^{-1} + 0.05u_0
T_0	293.15 K	0.1 K
T_{ref}	293.15–333.15 K	0.1 K
T_w	293.15–333.15 K	0.1 K
ρ_s	1190 kg m^{-3}	10 kg m^{-3}
c_s	1470 J (kg K)$^{-1}$	20 J (kg K)$^{-1}$
k_s	0.19 W (m K)$^{-1}$	0.01 W (m K)$^{-1}$
Δx	0.4 mm Pixel^{-1}	0.04 mm Pixel^{-1}

$$\begin{aligned} \delta h &= \Bigg(\left(\frac{\partial h}{\partial \dot{q}_w}\right)^2 [\delta\dot{q}_w]^2 + \left(\frac{\partial h}{\partial T_{ref}}\right)^2 [\delta T_{ref}]^2 \\ &\quad + \left(\frac{\partial h}{\partial T_w}\right)^2 [\delta T_w]^2 \Bigg)^{1/2} \\ &= \Bigg(\left(\frac{h}{\dot{q}_w}\right)^2 [\delta\dot{q}_w]^2 + \left(\frac{h}{T_{ref}-T_w}\right)^2 [\delta T_{ref}]^2 \\ &\quad + \left(\frac{h}{T_{ref}-T_w}\right)^2 [\delta T_w]^2 \Bigg)^{1/2}. \end{aligned} \qquad (20)$$
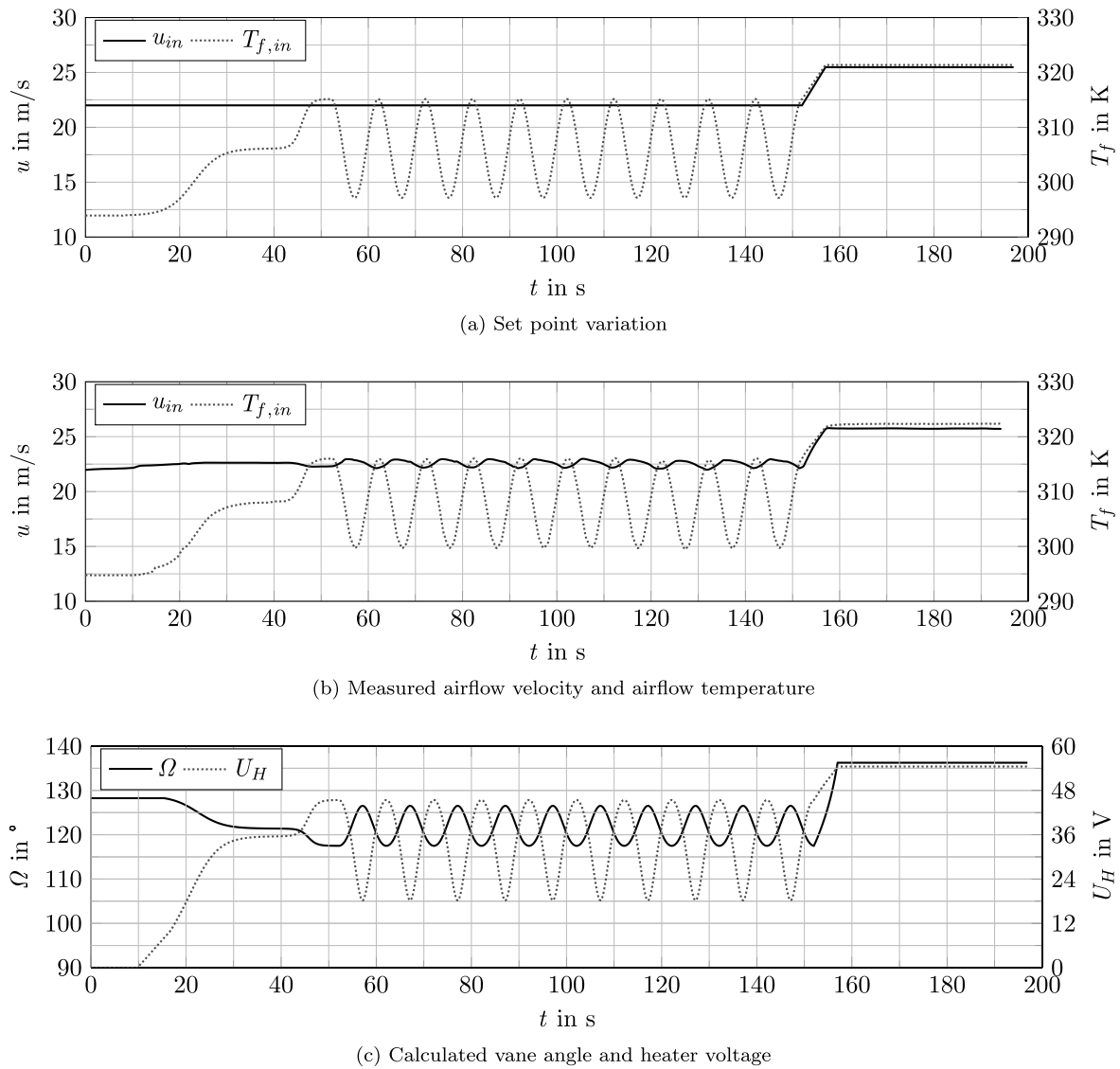
The quantities $\dot{q}_w$ and T_w are considered as independent of each other. For the experiments discussed in the results section, the relative uncertainties $\delta\dot{q}_w/\dot{q}_w$ and $\delta h/h$ vary between 10% to 15% on average. They are dependent on position and time. Furthermore, smaller $\dot{q}_w$ and h lead to larger relative uncertainties. The relative uncertainty $\delta h/h$ is affected also by the driving temperature difference $T_{ref}-T_w$. If $T_{ref}-T_w$ approaches zero, $\delta h/h$ tends to infinity. Further details are given in Brack (2020).

5. Results

To demonstrate the functionality and performance of the experimental setup as well as to visualize the possibilities of the evaluation method, the results of two different experiments are presented in the following. First, an experiment with a constant airflow velocity at a periodically pulsating airflow temperature is discussed. The frequency $\nu_{T_{f,in}}$ of the pulsation was set to 0.1 Hz. Then a second experiment is presented in which the airflow temperature maintained constant in sections and the airflow velocity pulsed continuously with a frequency $\nu_{u_{in}}$ of 0.05 Hz.

Both experiments represent generic ones. They are not derived from any explicit periodic phenomenon, e.g. in the secondary air system in gas turbine steady-state operation. However, both are particularly suited to demonstrate the performance, the repeatability, and the limitations of the experimental framework in single experiments. The frequencies of the two experiments with periods of several seconds are in the range in which unsteady, periodic and/or non-periodic, operating point changes can occur in turbomachinery (LaGraff *et al* 2006).

(a) Set point variation

(b) Measured airflow velocity and airflow temperature

(c) Calculated vane angle and heater voltage

Figure 10. Inlet airflow condition histories as well as control variable histories for the pulsing airflow temperature experiment.
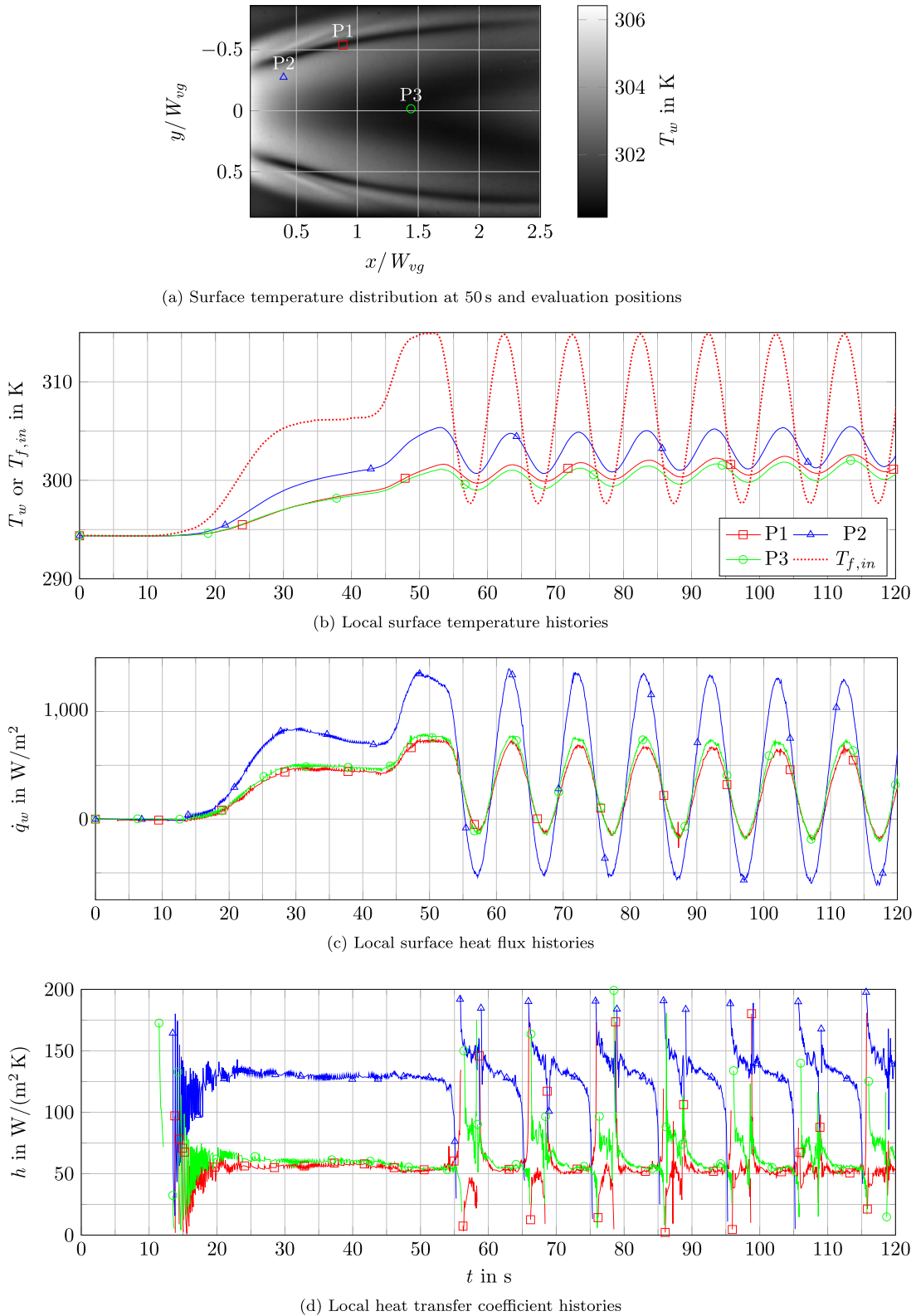
5.1. Pulsating airflow temperature

Figure 10(a) shows the predefined set point history for the pulsating airflow temperature experiment. Up to 152 s the airflow velocity keeps constant at 22 m s^{-1}. Then it increases linearly to the maximum value of 25.47 m s^{-1} and stays constant again. The temporal set point variation of the airflow temperature starts with an S-shaped increase from ambient conditions to a value of 306.15 K after 14 s. After reaching the higher temperature level, the airflow temperature pulsates with an amplitude of 9 K around the average value of 306.25 K at a frequency of 0.1 Hz. This pulsation lasts up to 152 s. Then the airflow temperature linearly increases to the maximum temperature level of 321.36 K.

This predefined set point history served as input to calculate the temporal variation of Ω and U_H, which are shown in figure 10(c). The main varying control variable is U_H. However, even if only $T_{f,in}$ changes up to 152 s, this requires not only a variation of the U_H, but also a variation of Ω at the same

time. The changes of Ω and U_H are antagonistic. An increase in U_H gives a reduction in Ω and vice versa.

The measured histories of u_{in} and $T_{f,in}$ are plotted in figure 10(b). A comparison with the set point history of figure 10(a) confirms a good agreement with only minor deviations. The inlet velocity u_{in} reaches a mean value of 22.6 m s^{-1} up to 152 s and pulsates slightly with an amplitude smaller than 0.4 m s^{-1}. The airflow control system also reproduces the rapid linear rise afterwards. A slight overshoot is visible. As described in section 2.4, this part of the experiment only aims at evaluating the complete experiment duration with a pulsating flow temperature. An evaluation of the heat transfer of the section after 152 s is not carried out.

Between the measured value and the set point value of $T_{f,in}$ a constant offset of 0.82 K exists. It results from an increased ambient temperature between the point in time of the measurement of the operating range and the point in time of the actual experiment. During pulsation the maxima reach an average value of 315.88 K and the minima are on average 299.63 K.

(a) Surface temperature distribution at 50 s and evaluation positions

(b) Local surface temperature histories

(c) Local surface heat flux histories

(d) Local heat transfer coefficient histories

Figure 11. Local heat transfer data for the pulsation airflow temperature experiment with $\nu_{T_{f,in}} = 0.1$ Hz.

The maxima deviate from the average value not more than 0.1 K and the minima not more than 0.2 K. Thus the average amplitude is 8.13 K which deviates 0.87 K from the set point.

The effects of the airflow temperature pulsation at a constant airflow velocity on the heat transfer are illustrated in figure 11. Figure 11(a) visualizes the position of the the local points for evaluation with a contour plot of the surface

temperature at 50 s. Due to the longitudinal vortex system with main vortices, corner vortices as well as a horseshoe vortex, the surface temperature in the wake of the VG has a specific characteristic. It consists of two streaks of high temperature and a streak of lower temperature in between on each side of the symmetry plane. Position P1 is located in the upwash area between the main and the corner vortex. In this area the heat transfer is in principle lower than in the downwash areas of the vortexes where the evaluation point P2 is located. Therefore, downwash areas have a higher surface temperature than other areas and are visible behind the VG as high temperature streaks. Location P3 is in a region of lower heat transfer on the symmetry plane between the two main vortices.

Independent of the local position, T_w starts to increase as soon as $T_{f,in}$ starts to increase from the temperature of thermal equilibrium to a higher temperature level (see figure 11(b)). Dependent on the local strength of the heat transfer, the strength of the local temperature rise of T_w varies. Due to the fact that P2 is located directly in the downstream region of the main vortex and close to the VG, T_w rises significantly faster than at P1 and P3. The strength of the T_w temperature rise at P1 and P3 is almost equal.

As the surface heat flux $\dot{q}_w$, shown in figure 11(c), is the root cause for the temporal change of T_w, it changes the strongest where T_w also changes the strongest. In conclusion, at the beginning $\dot{q}_w$ shows the strongest increase at P2 and with superimposed pulsation of $T_{f,in}$ also the strongest amplitude.

Figure 11(d) shows the histories of the calculated heat transfer coefficient h at the positions P1 to P3. Regardless of the position, h cannot be determined up to 14 s after the beginning of the experiment, since the driving temperature difference and $\dot{q}_w$ are zero. After 14 s $\dot{q}_w$ increases, but the driving temperature difference is still small, which leads to strongly fluctuating heat transfer coefficients. Smallest measurement errors have a strong effect on h. After approximately 25 s the heat transfer coefficient stabilizes at a constant value. Here, the already discussed differences in the strength of the heat transfer become apparent. At P2, h reaches a value of 130 W$(m^2 K)^{-1}$, while P3 has a value of 60 W$(m^2 K)^{-1}$ and P1 a value of 56 W$(m^2 K)^{-1}$, which is significantly lower.

With starting pulsation of $T_{f,in}$, h changes in time. Due to the large change in flow temperature, two different phases of surface heat flux direction occur. A phase with a negative driving temperature difference results in a negative surface heat flux and a phase with a positive driving temperature difference results in a positive surface heat flux. During phases with a positive driving temperature difference h stabilizes for P1 and P3. However, for P2 h continuously changes.

5.2. Pulsating airflow velocity

The inlet conditions of the pulsating airflow experiment and the therefore required variation of Ω and U_H are visualized in figure 12 up to 120 s. Figure 12(a) shows the defined set point variation of u_{in} and $T_{f,in}$. Right at the beginning of the experiment u_{in} starts to pulsate with a frequency of 0.05 Hz and an amplitude of 5 m s^{-1} around the mean inlet velocity of 15 m s^{-1}. As for the pulsating airflow temperature experiment, $T_{f,in}$ increases in an S-shaped form from ambient conditions to a value of 310.65 K after 25 s. When reaching a $T_{f,in}$ of 310.65 K it keeps constant.

Figure 12(c) presents the calculated temporal variation of Ω and U_H using the defined set point histories of u_{in} and $T_{f,in}$ as well as the operating range of the experimental setup. Compared to the pulsing airflow temperature experiment, the required pulsation amplitude of Ω increases. Furthermore, the non-sinusoidal shape of the Ω pulsation visualizes the non-linear relationship between u_{in} and Ω.

When reaching the constant $T_{f,in}$ of 310.65 K, the pulsation of u_{in} requires a significant pulsation of U_H too. This pulsation of U_H reaches with an amplitude of approximately 6 V the same range as for the pulsating temperature experiment.

The measured u_{in} and $T_{f,in}$ are plotted in the graph of figure 12(b). Also for this experiment a good agreement between set point histories and measured histories exists. Minor deviations are visible for the extremas of u_{in}. The average maximum of u_{in} is 20.25 m s^{-1} and the average minimum is 10.05 m s^{-1}. These average values are met in a stable manner each pulsation period.

Furthermore, $T_{f,in}$ does not reach a fully constant value of 310.65 K but pulsates slightly due to the interaction of changing velocity and electrical heater control.

Figure 13 visualizes the position of five different line profiles in the wake of the VG in order to present the influence of the pulsation airflow velocity on the heat transfer.

Figure 14 shows the corresponding heat transfer coefficient distributions along the five different line profiles and their variation with time for six different points in time. With figure 14(b) the illustration starts at the maximum u_{in} and ends with figure 14(g) one period further at the maximum u_{in}.

In general and independent of the considered line, the heat transfer coefficient decreases with decreasing u_{in} and increases with increasing u_{in}. In addition, for the lines 1 to 3 the shape of the h-profile is not influenced too. Each profile characterizes four main maxima and three main minima which vary in their absolute value and their y/W_{vg}-position. For the lines 4 and 5 the general shape changes with time and u_{in}. At $t = 55$ s the h-profile of line 5 has a clear maxima at $y/W_{vg} = 0$. The h-profile of line 4 shows for same point in time and position a plateau. With decreasing u_{in} the maxima of the h-profile of line 5 almost vanishes and the plateau of line 4 gets shorter. As the local maximum in heat transfer at line 5 in the center position occurs only at the maximum u_{in}, it indicates a change in local flow field structures.
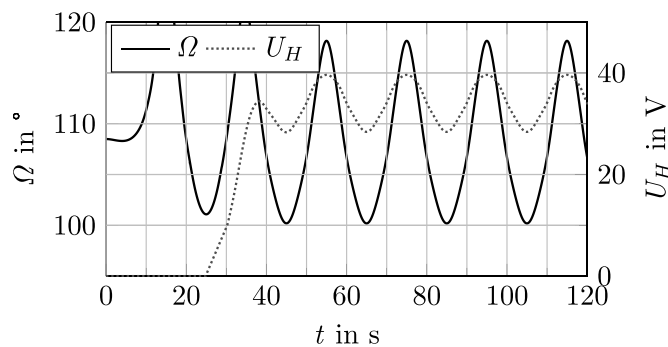
After a period, the same h-profiles result as at the beginning of the period.
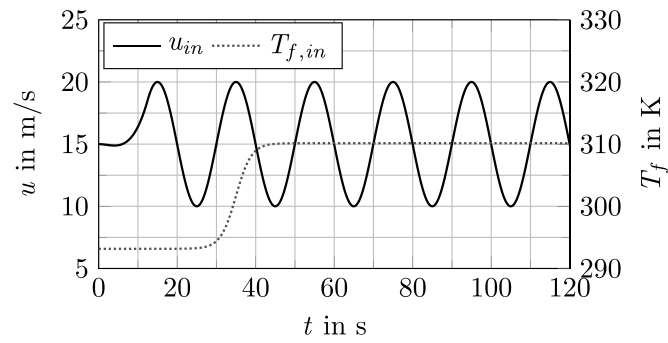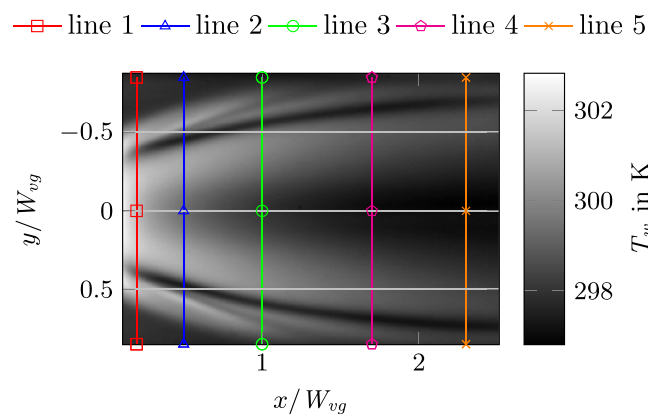
(a) Set point variation
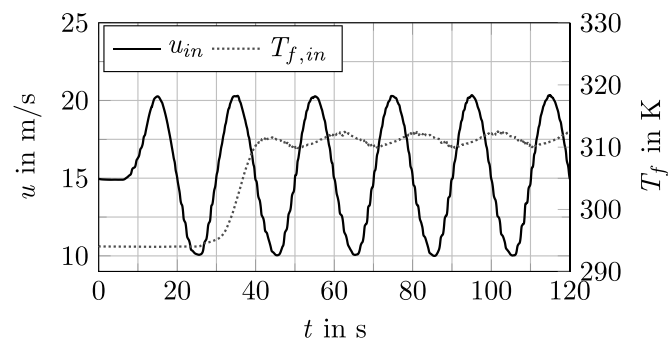
(b) Measured airflow velocity and airflow temperature
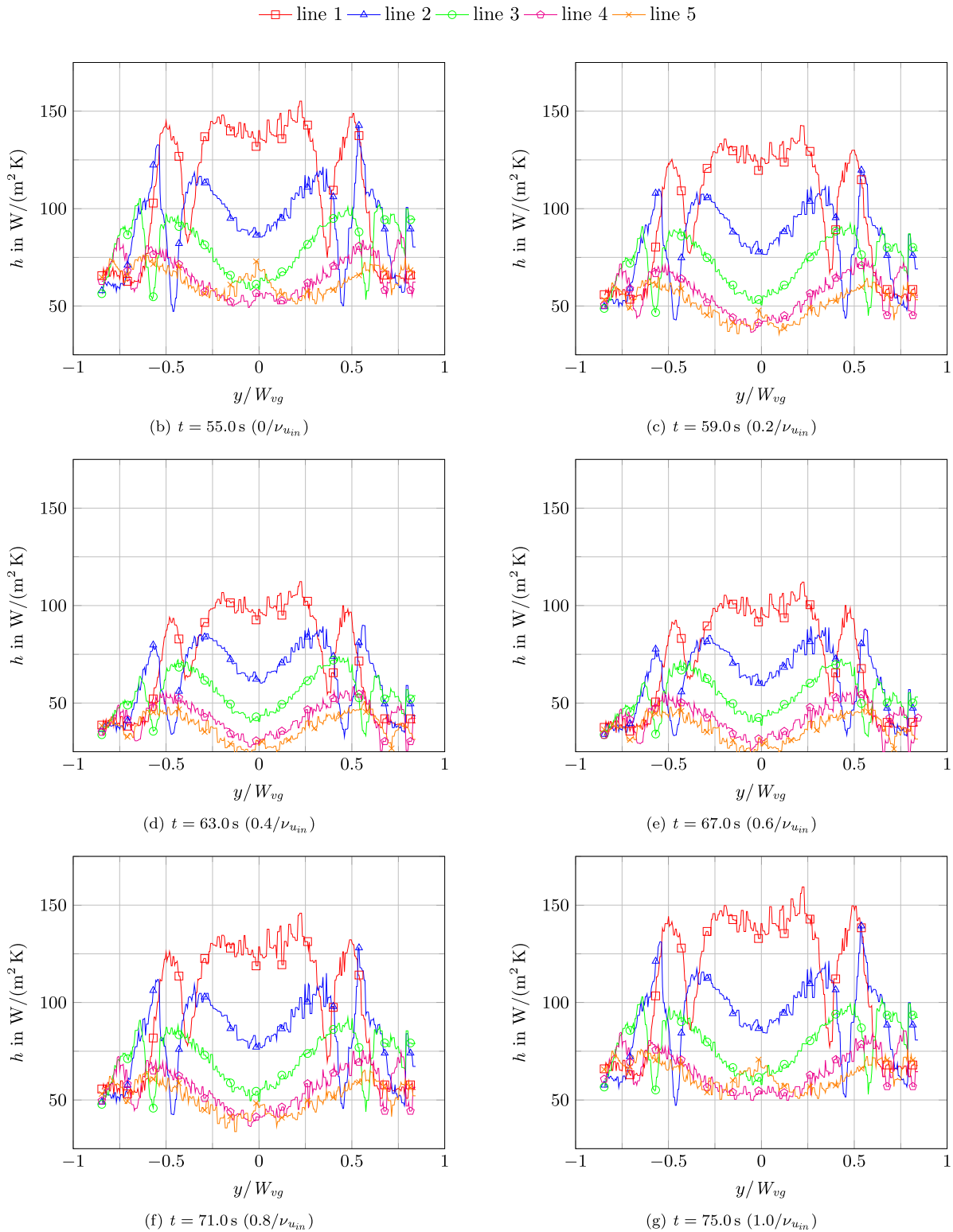

(c) Calculated vane angle and heater voltage

Figure 12. Inlet airflow condition histories as well as control variable histories for the pulsing airflow velocity experiment.

Figure 13. Surface temperature distribution at 50 s and evaluation position of line profiles.

(b) $t = 55.0\,\mathrm{s}\ (0/\nu_{u_{in}})$

(c) $t = 59.0\,\mathrm{s}\ (0.2/\nu_{u_{in}})$

(d) $t = 63.0\,\mathrm{s}\ (0.4/\nu_{u_{in}})$

(e) $t = 67.0\,\mathrm{s}\ (0.6/\nu_{u_{in}})$

(f) $t = 71.0\,\mathrm{s}\ (0.8/\nu_{u_{in}})$

(g) $t = 75.0\,\mathrm{s}\ (1.0/\nu_{u_{in}})$

Figure 14. Heat transfer coefficient line profiles for different points in time during airflow velocity pulsation.

6. Conclusion

This paper summarizes two major contributions. First, an experimental setup for unsteady convective heat transfer experiments is presented that allows these experiments to be conducted in a deterministic and repeatable manner. Second, a measurement and evaluation methodology is discussed which provides measurement data with high accuracy and heat transfer evaluation data which is temporally and spatially resolved.

The airflow control system, consisting of a mesh heater and adjustable vanes, provides a simple and easy-to-implement

setup to independently change the airflow temperature and the airflow velocity of a channel flow. The presented experimental results show that the precalculation of the temporal course of the control variables using the steady-state operating range works well. The deviations are smaller than $0.4\,\mathrm{m\,s^{-1}}$ for u_{in} and $0.2\,\mathrm{K}$ for $T_{f,in}$. Also, the pulsation frequencies set before the experiment are accurately matched. The described airflow control system does not completely succeed in keeping either u_{in} constant during a $T_{f,in}$ change or vice versa. Some transient effects are not taken into account in the precalculation of the control variables, as e.g. the thermal inertia of the mesh heater. Further, the power supply units and the electric motor exhibit inertia in their control.

With the presented evaluation method, evaluation quantities of the heat transfer are obtained whose uncertainty of 10%–15% is comparable to other transient evaluation methods, for example the transient TLC method. The resolution of all evaluation values enables further analysis of the time dependent heat transfer characteristics.

Data availability statement

The data that support the findings of this study are available upon reasonable request from the authors.

ORCID iD

Stefan Brack ⓘ https://orcid.org/0000-0002-7010-4804

References

Abudu K, Igie U, Roumeliotis I and Hamilton R 2021 Impact of gas turbine flexibility improvements on combined cycle gas turbine performance *Appl. Therm. Eng.* **189** 116703

Bons J 2009 Transient method for convective heat transfer measurement with lateral conduction—part I: application to a deposit-roughened gas turbine surface *J. Heat Transfer* **131** 011301

Bons J, Fletcher D and Borchert B 2009 Transient method for convective heat transfer measurement with lateral conduction—part II: application to an isolated spherical roughness element *J. Heat Transfer* **131** 011302

Brack S 2020 Time-resolved transient convective and conjugate heat transfer experiments using IR thermography *PhD Thesis* Institute of Aerospace Thermodynamics, University of Stuttgart

Brack S, Poser R and von Wolfersdorf J 2017 A comparison between transient heat transfer measurement using TLC and IR thermography *World Conf. on Experimental Heat Transfer, Fluid Mechanics and Thermodynamics (September 2017, Iguazu Falls, Brazil)*

Coulthard S M, Volino R J and Flack K A 2007 Effect of jet pulsing on film cooling—part I: effectiveness and flow-field temperature results *J. Turbomach.* **129** 232

Durst F, Heim U, Ünsal B and Kullik G 2003 Mass flow rate control system for time-dependent laminar and turbulent flow investigations *Meas. Sci. Technol.* **14** 893–902

Elshafei E A, Mohamed M S, Mansour H and Sakr M 2008 Experimental study of heat transfer in pulsating turbulent flow in a pipe *Int. J. Heat Fluid Flow* **29** 1029–38

Estorf M 2006 Image based heating rate calculation from thermographic data considering lateral heat conduction *Int. J. Heat Mass Transfer* **49** 2545–56

Fallen M 1982 Waermeuebergang im Rohr mit ueberlagerter Stroemungspulsation *Waerme- Stoffuebertrag.* **16** 89–99

Galoul V, Reulet P, Laroche E and Millan P 2010 Experimental and numerical investigation of an unsteady conjugate heat transfer case *10th AIAA/ASME Joint Thermophysics and Heat Conf.* (American Institute of Aeronautics and Astronautics)

Gompertz K, Jensen C, Kumar P, Peng D, Gregory J W and Bons J P 2011 Modification of transonic blowdown wind tunnel to produce oscillating freestream mach number *AIAA J.* **49** 2555–63

Habib M A, Attya A M, Eid A I and Aly A Z 2002 Convective heat transfer characteristics of laminar pulsating pipe air flow *Heat Mass Transfer* **38** 221–32

Ireland P T, Neely A J, Gillespie D R and Robertson A J 1999 Turbulent heat transfer measurements using liquid crystals *Int. J. Heat Fluid Flow* **20** 355–67

Jensen C, Gompertz K, Peng D, Juliano T, Kumar P, Gregory J and Bons J 2011 Unsteady compressible flow on a NACA 0021 airfoil *49th AIAA Aerospace Sciences Meeting Including the New Horizons Forum and Aerospace Exposition* (American Institute of Aeronautics and Astronautics)

Ji T H, Kim S Y and Hyun J M 2008 Experiments on heat transfer enhancement from a heated square cylinder in a pulsating channel flow *Int. J. Heat Mass Transfer* **51** 1130–8

Kuželka J, Nesládek M, Lutovinov M, Jurenka J, Růžička M, Rund M and Měšťánek P 2019 Numerical simulations of fatigue crack growth in a steam turbine rotor blade groove *Proc. Struct. Integr.* **17** 780–7

LaGraff J E, Ashpis D E, Oldfield M L and Gostelow J P 2006 *Minnowbrook V 2006 Workshop on Unsteady Flows in Turbomachinery* NASA/CP-2006-214484

Lalizel G, Sultan Q, Fénot M and Dorignac E 2012 Experimental convective heat transfer characterization of pulsating jet in cross flow: influence of Strouhal number excitation on film cooling effectiveness *J. Phys.: Conf. Series* **395** 012043

Li G, Zheng Y, Hu G and Zhang Z 2013 Heat transfer enhancement from a rectangular flat plate with constant heat flux in pulsating flows *Exp. Heat Transfer* **27** 198–211

Liu C, von Wolfersdorf J and Zhai Y N 2014 Time-resolved heat transfer characteristics for steady turbulent flow with step changing and periodically pulsating flow temperatures *Int. J. Heat Mass Transfer* **76** 184–98

Liu C, von Wolfersdorf J and Zhai Y N 2015 Time-resolved heat transfer characteristics for periodically pulsating turbulent flows with time varying flow temperatures *Int. J. Therm. Sci.* **89** 222–33

Magni F, Grimm F, Sorato S and Micheli M 2016 GT13E2 low part load operation: extended flexibility down to 30% load *Coal, Biomass and Alternative Fuels; Cycle Innovations; Electric Power; Industrial and Cogeneration; Organic Rankine Cycle Power Systems* vol 3 (American Society of Mechanical Engineers)

Moffat R J 1982 Contributions to the theory of single-sample uncertainty analysis *J. Fluids Eng.* **104** 250

Moon J W, Kim S Y and Cho H H 2005 Frequency-dependent heat transfer enhancement from rectangular heated block array in a pulsating channel flow *Int. J. Heat Mass Transfer* **48** 4904–13

Newton P J, Yan Y, Stevens N E, Evatt S T, Lock G D and Owen J 2003 Transient heat transfer measurements using thermochromic liquid crystal. Part 1: an improved technique *Int. J. Heat Fluid Flow* **24** 14–22

Özisik M N 1985 *Heat Transfer: A Basic Approach* (New York: McGraw-Hill)

Park J S, Taylor M F and McEligot D M 1982 Heat transfer to pulsating, turbulent gas flow *Proc. 7th International Heat Transfer Conference* (*Munich*) vol 3 pp 105–10

Persoons T, Saenen T, Oevelen T V and Baelmans M 2012 Effect of flow pulsation on the heat transfer performance of a minichannel heat sink *J. Heat Transfer* **134** 091702

Poser R and von Wolfersdorf J 2011 Liquid crystal thermography for transient heat transfer measurements in complex internal cooling systems *Heat Transfer Res.* **42** 181–97

Poser R, von Wolfersdorf J and Semmler K 2005 Transient heat transfer experiments in complex passages *Proc. ASME 2005 Summer Heat Transfer Conference collocated with the ASME 2005 Pacific Rim Technical Conf. and Exhibition on Integration and Packaging of MEMS, NEMS, and Electronic Systems* (*San Francisco, California, USA, 17–22 July 2005*) vol 1 pp 797–804

Schultz D and Jones T 1973 Heat-transfer measurements in short-duration hypersonic facilities *AGARDograph* **165** 1–157

Sheriff H S and Zumbrunnen D A 1994 Effect of flow pulsations on the cooling effectiveness of an impinging jet *J. Heat Transfer* **116** 886

Ünsal B and Durst F 2006 Pulsating flows: experimental equipment and its application *JSME Int. J.* B **49** 980–7

Zohir A E, Habib M A, Attya A M and Eid A I 2005 An experimental investigation of heat transfer to pulsating pipe air flow with different amplitudes *Heat Mass Transfer* **42** 625–35